Photosensitizer-Loaded Gold Vesicles with Strong Plasmonic Coupling Effect for Imaging-Guided Photothermal/Photodynamic Therapy

Jing Lin,[†,§,#] Shouju Wang,[‡,⊥,#] Peng Huang,[‡,§,#] Zhe Wang,[‡,∥] Shouhui Chen,[‡,§] Gang Niu,[‡] Wanwan Li,[‡] Jie He,[†] Daxiang Cui,[§] Guangming Lu,[⊥] Xiaoyuan Chen,[‡,*] and Zhihong Nie[†,*]

[†]Department of Chemistry and Biochemistry, University of Maryland, College Park, Maryland 20742, United States, [‡]Laboratory of Molecular Imaging and Nanomedicine (LOMIN), National Institute of Biomedical Imaging and Bioengineering (NIBIB), National Institutes of Health, Bethesda, Maryland 20892, United States, [§]Institute of Micro-Nano Science and Technology, Shanghai Jiao Tong University, Shanghai 200240, China, [⊥]Jinling Hospital, Clinical School of Medical College, Nanjing University, Nanjing, 210000, China, and [∥]Center for Molecular Imaging and Translational Medicine, School of Public Health, Xiamen University, Xiamen 361005, China. [#]These authors contributed equally to this article.

ABSTRACT A multifunctional theranostic platform based on photosensitizer-loaded plasmonic vesicular assemblies of gold nanoparticles (GNPs) is developed for effective cancer imaging and treatment. The gold vesicles (GVs) composed of a monolayer of assembled GNPs show strong absorbance in the near-infrared (NIR) range of 650−800 nm, as a result of the plasmonic coupling effect between neighboring GNPs in the vesicular membranes. The strong NIR absorption and the capability of encapsulating photosensitizer Ce6 in GVs enable trimodality NIR fluorescence/thermal/photoacoustic imaging-guided synergistic photothermal/photodynamic therapy (PTT/PDT) with improved efficacy. The Ce6-loaded GVs (GV-Ce6) have the following characteristics: (i) high Ce6 loading efficiency (up to ~18.4 wt %; (ii) enhanced cellular uptake efficiency of Ce6; (iii) simultaneous trimodality NIR fluorescence/thermal/photoacoustic imaging; (iv) synergistic PTT/PDT treatment with improved efficacy using single wavelength continuous wave laser irradiation.

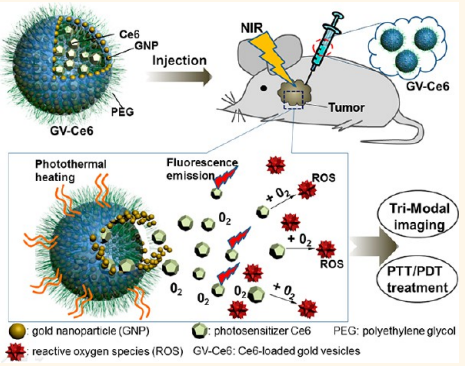

KEYWORDS: gold vesicles · plasmonic coupling effect · photoacoustic imaging · photothermal therapy · photodynamic therapy · synergistic therapy

Photodynamic therapy (PDT) is an extraordinary theranostic modality for various malignant and nonmalignant diseases.[1−8] This approach utilizes reactive oxygen species (ROS) generated through the reaction between photosensitizer (PS) and oxygen presented in tissues upon the irradiation of light to achieve effective treatment.[9−12] However, the PDT efficacy of solid tumors is largely limited by issues including: (i) inadequate selectivity of most PSs;[13−16] (ii) poor water-solubility of most PSs;[17−21] (iii) self-destruction of PSs upon light irradiation;[22] and (iv) ceasing production of singlet oxygen (SO) due to severe local hypoxia caused by the depletion of tissue oxygen and disruption of tumor blood flow.[23,24] New synergistic treatment modalities, which combine PDT with other therapies such as photothermal therapy (PTT), hold the promise to overcome current limitations of PDT, thus achieving enhanced anticancer efficacy.[25−31] Generally, individual nanoparticles (NPs) such as gold nanorods (GNRs),[27,29] carbon nanohorns[32] and graphene oxide[12] complexed with PSs on their surface are used to promote the tumor accumulation of PSs and to generate heat for synergistic PDT/PTT. However, this method has limitations including relatively low loading capacity of PSs due to limited surface area of NPs and the possible leakage of PSs coupled/complexed on NP surfaces during their circulation in biological systems.[33] In addition, PDT/PTT based on photothermal coupling agents (PTCAs)/PSs usually need two lasers in different wavelengths due to the absorption mismatch of PTCAs

* Address correspondence to znie@umd.edu, Shawn.Chen@nih.gov.

Received for review March 7, 2013 and accepted May 23, 2013.

Published online May 23, 2013
10.1021/nn4011686

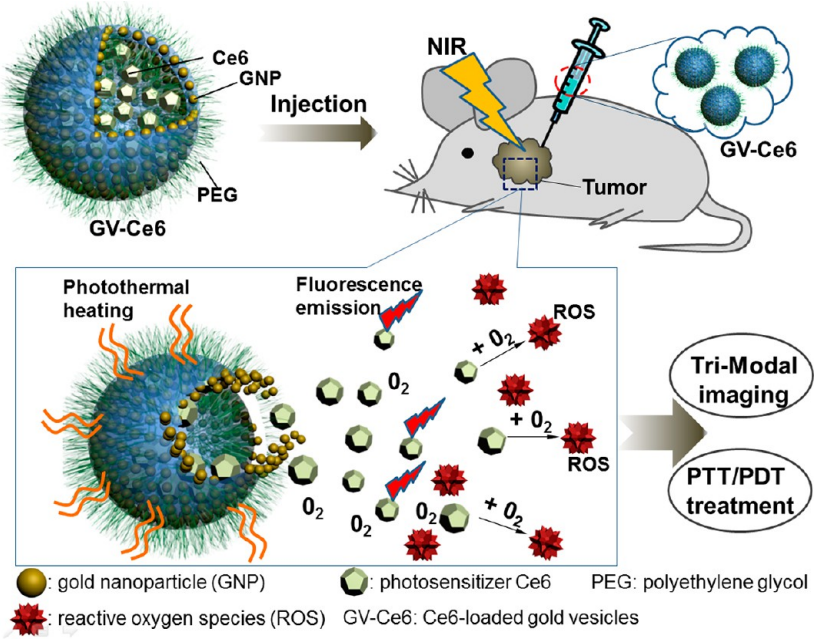

Scheme 1. Photosensitizer (Ce6)-Loaded Plasmonic Gold Vesicles (GVs) for Trimodality Fluorescence/Thermal/Photoacoustic Imaging Guided Synergistic Photothermal/Photodynamic Cancer therapy

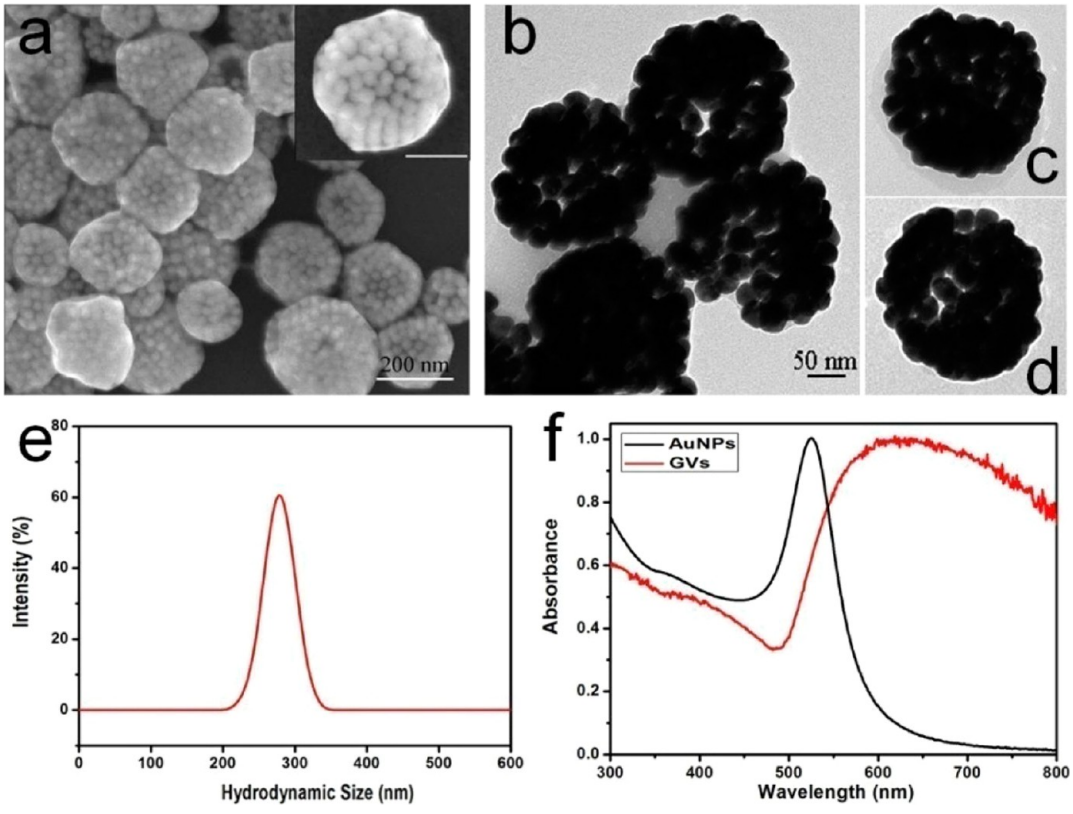

Figure 1. (a) SEM and (b–d) TEM images of plasmonic gold vesicles (GVs) self-assembled from GNPs. (e) Size distribution of GVs by DLS; (d) UV–vis spectra of BCP-tethered GNPs and GVs.

and PSs.[12,27] The sequential irradiation prolongs the treatment time and requires precise alignment of the two light beams. Therefore, there still remains a grand challenge to develop a simple yet effective strategy for simultaneous synergistic PDT/PTT treatment.

Here we report the design of multifunctional photosensitizer Ce6-loaded plasmonic gold vesicles (GVs) for

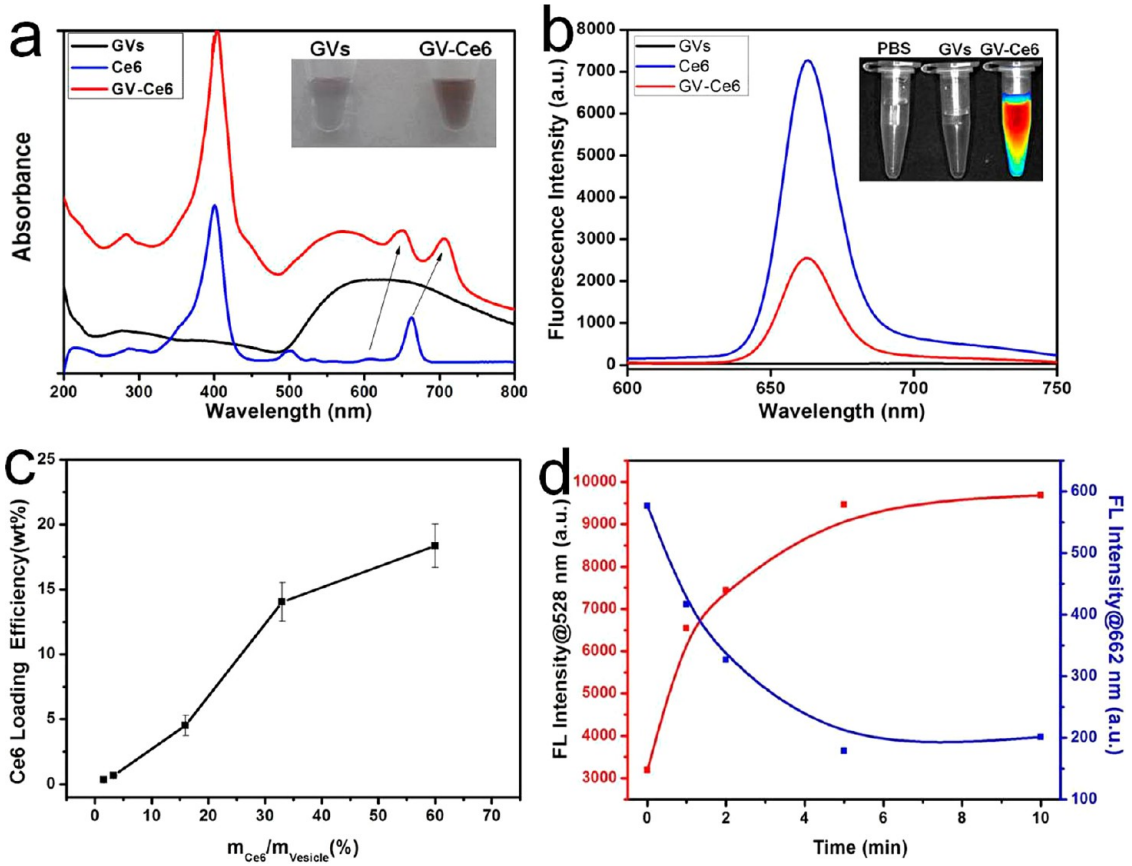

Figure 2. (a) UV−vis spectra of GVs (black), Ce6 (blue) and GV-Ce6 (red). The arrows indicate characteristic Q-bands of Ce6; (b) fluorescence emission spectra of GVs, Ce6 and GV-Ce6; (c) Ce6 loading efficiency of GV-Ce6 as a function of Ce6 concentration; (d) the changes of fluorescence intensity at the characteristic peaks of SOSG and Ce6 (528 and 662 nm) as a function of laser irradiation time.

trimodality fluorescence/thermal/photoacoustic (PA) imaging guided synergistic PTT/PDT cancer treatment. The GVs composed of a monolayer of assembled gold nanoparticles (GNPs) show a strong absorbance in the NIR range of 650−800 nm, as a result of the plasmonic coupling between neighboring GNPs in the vesicular membranes.[34−37] This enables the use of 671 nm laser irradiation to simultaneously excite both GVs and Ce6 to produce heat and SO, killing cancer cells (Scheme 1). The heating effect upon laser irradiation dissociates the Ce6-loaded GVs (GV-Ce6) to release the encapsulated Ce6 molecules. The efficient loading of Ce6 in GVs significantly increases the accumulation of Ce6 in cancer cells. The tumor tissues visualized by the fluorescence, thermal and PA signals from GV-Ce6 can be selectively destroyed in a noninvasive manner by the illumination of 671 nm laser. Both *in vitro* and *in vivo* therapeutic efficacy of GV-Ce6 were enhanced compared to either individual PTT or PDT alone, or the sum of PTT/PDT due to the synergistic effect.

RESULTS AND DISCUSSION

Plasmonic GVs were prepared by assembling GNPs tethered with amphiphilic block copolymers (BCPs)[38] (see details in Supporting Information). GNPs were prepared by citrate reduction of $HAuCl_4$ in aqueous phase. GNPs with a diameter of 26.2 ± 1.45 nm were modified with thiol-terminated BCPs of polyethylene oxide-*b*-polystyrene (PEO_{45}-*b*-PS_{245}) (M_n = 25.7 kg/mol, PDI = 1.12). The self-assembly of the BCP-tethered GNPs was triggered by the rehydration of a film of GNPs in water under sonication. To encapsulate Ce6 in the GVs, an aqueous solution of Ce6 with a predetermined concentration was used for the rehydration process. Representative scanning electron microscopy (SEM) and transmission electron microscopy (TEM) images shown in Figure 1a,b present the well-defined vesicular assemblies of GNPs (see Figure S1 and S2 for more images). The hollow interior of the assemblies was confirmed by the penetration of electron beam through the GVs, and the morphology of broken or collapsed GVs (Figure S3). The GVs are composed of a monolayer shell of densely packed GNPs (Figure 1a−d). The GVs exhibit a relatively narrow size distribution and the average size of GVs is 281.4 ± 62.3 nm, as shown in dynamic light scattering (DLS) analysis (Figure 1e). Assembly of GNPs significantly reduced the interparticle distance, leading to a red-shift in extinction spectra due to enhanced plasmonic coupling between adjacent GNPs. Upon the formation of GVs, the localized

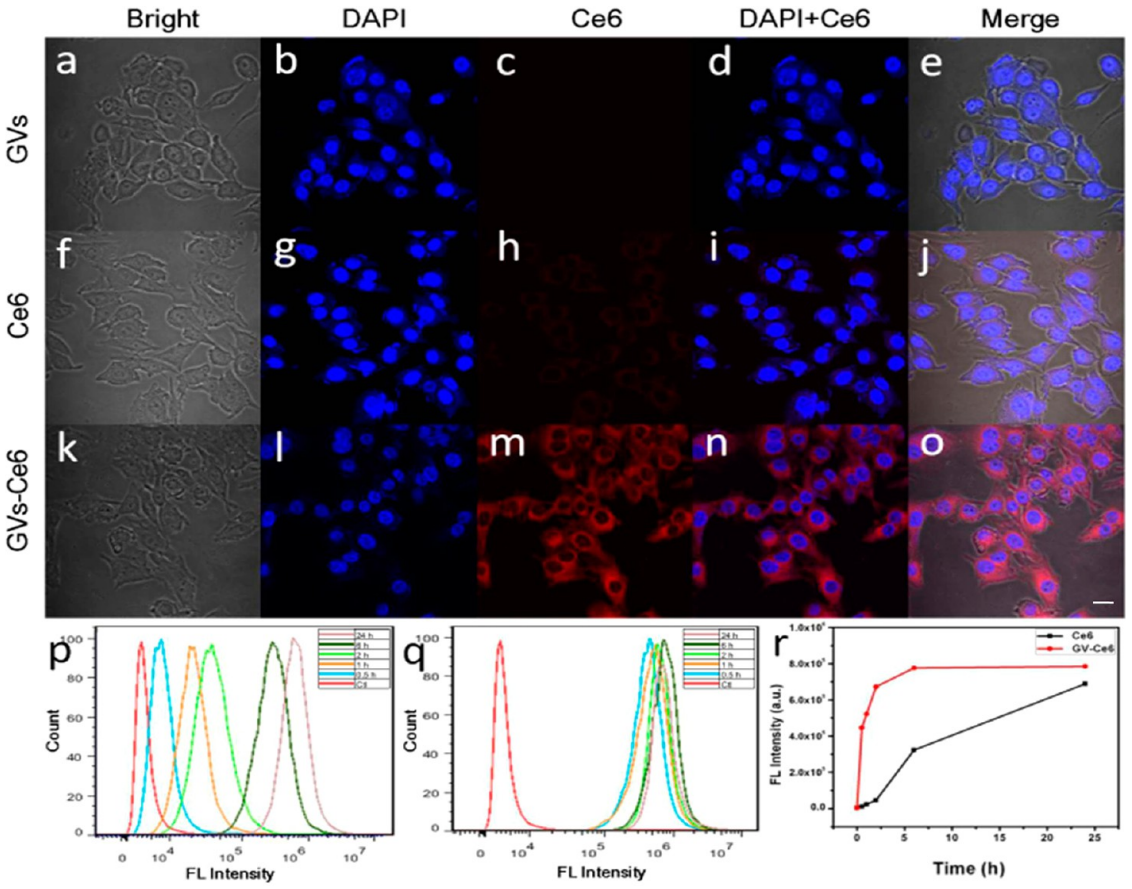

Figure 3. Subcellular localization of GVs (a−e), Ce6 (f−j) and GV-Ce6 (k−t) in MDA-MB-435 cells. (a, f, k) Bright field; (b, g, l) nuclei fluorescence (DAPI); (c, h, m) Ce6 fluorescence; (d, i, n) merged images of b and c, g and h, l and m; (e, j, o) merged images of a, b, and c; f, g, and h; k, l, and m. The scale bar is 20 μm. (p and q) Ce6 fluorescence in cells after incubation with pure Ce6 (p) and GV-Ce6 (q) at different time points; (r) the changes of Ce6 fluorescence intensity in cells as a function of incubation time.

surface plasmon resonance (LSPR) peak shifted from 518 to 630 nm and broadened to cover the wavelength range of 650−800 nm (Figure 1f). The strong absorption of GVs in NIR range implies the potential use of GVs as photothermal agents. We, therefore, chose to encapsulate photosensitizer Ce6 which can be excited for PDT upon 671 nm laser irradiation. We expect that the synergistic PTT and PDT will be achieved upon irradiating GV-Ce6 complex with 671 nm laser.

Successful loading of Ce6 in GVs was confirmed by UV−vis absorbance and fluorescence emission spectra. After loading Ce6, the absorption of GV-Ce6 displays the characteristic Soret peak of Ce6 at 404 nm, and the Q-bands at 651 and 706 nm (Figure 2a),[18] along with a color change of the solution from blue to dark black (Figure 2a, inset). The characteristic peaks of Ce6 loaded by GVs are not totally matching with the peaks of pure Ce6, which is attributed to the interaction between Ce6 and GVs. Meanwhile, we also observed that the fluorescence of Ce6 was markedly quenched once it was loaded by GVs (Figure 2b). The drug loading efficiency of Ce6 in GVs was quantified by using the UV−vis calibration curve of Ce6 at 663 nm (see Figure S4). When the weight ratio of Ce6 to GVs is 33%, the loading efficiency of Ce6 is ~14.1 wt % (Figure 2c). At a weight ratio of 60%, the Ce6 loading efficiency is up to 18.4 wt %. For a comparison, positively charged GNRs (with LSPR at ~671 nm) as control were used to load negatively charged Ce6 by electrostatic interactions between GNRs and Ce6. The maximum loading efficiency of Ce6 onto the GNRs is less than 10 wt % (Figure S5). This indicates that GVs can overcome the surface-area-limited drug loading on NPs by offering a large interior space to maximize loading capacity.[33]

To evaluate the efficiency of photothermal heating of GV-Ce6, solutions of different samples were exposed to 671 nm laser at 2.0 W/cm^2 (the same laser wavelength and intensity was used in all the experiments). The temperature of GVs and GV-Ce6 solutions rose rapidly over 42 °C within 5 min, while PBS and pure Ce6 solutions exhibit negligible increase in temperature (Figure S6). GV-Ce6 produced higher heating effect than GV alone, due to the absorbance of loaded Ce6 in GV-Ce6 at 671 nm. Under the same optical density (OD) absorbance of GNRs and GV-Ce6 at 671 nm, the efficiency of photothermal heating of GV-Ce6 is comparable to that of above-metioned GNRs (see Figure S7). These results suggest that GV-Ce6 can be used as

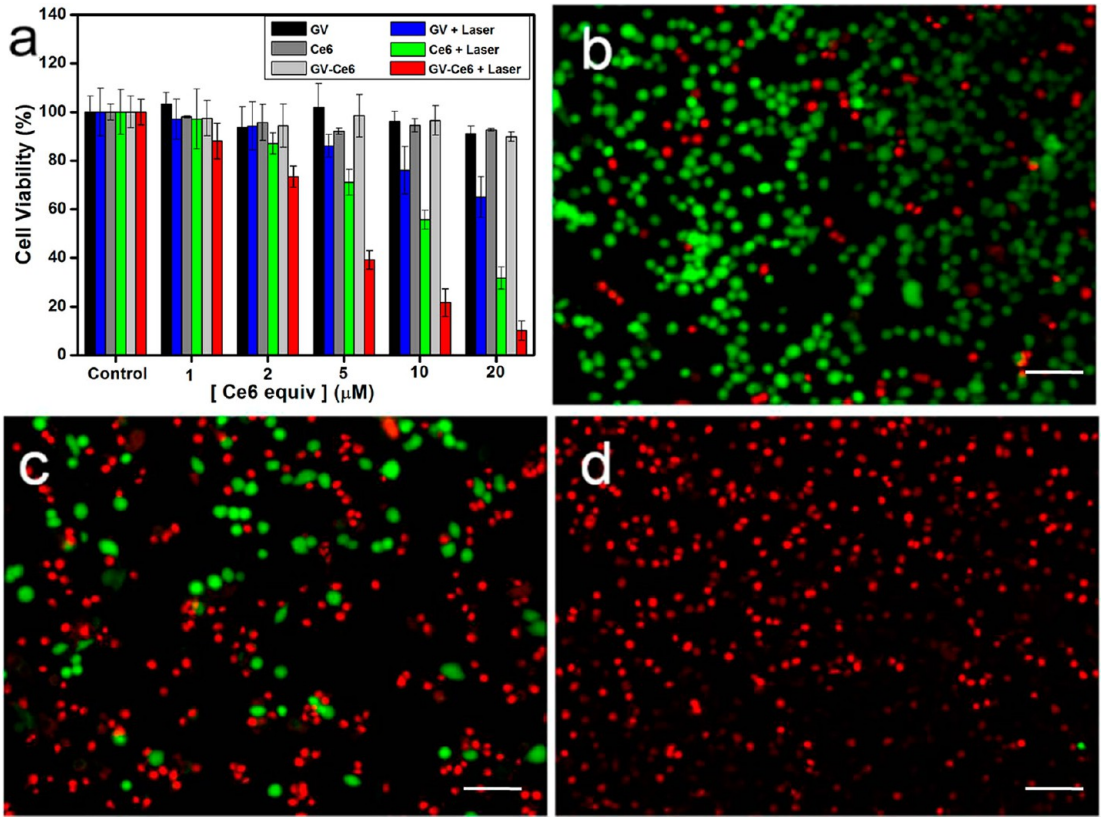

Figure 4. (a) MDA-MB-435 cell viability at different concentrations of GVs, Ce6, and GV-Ce6 for 12 h at 37 °C with or without irradiation for 3 min with a 671 nm laser (2 W/cm^2). Fluorescence images of Calcein AM and Ethidium homodimer-1 co-staining cancer cells incubated with (b) GVs (36.8 μg/mL), (c) Ce6 (10 μM), and (d) GV-Ce6 at a Ce6 concentration of 10 μM for 12 h at 37 °C after irradiation. Scale bars: 50 μm.

PTCAs for efficient PTT, while it has a higher loading capacity of Ce6 for PDT than GNR systems. The assembled GVs can be dissociated to release Ce6 encapsulated in the hollow cavity of GVs upon laser irradiation, thus achieving efficient PDT treatment (Figure S8). The generation of SO from GV-Ce6 was quantified by measuring the fluorescence signal of singlet oxygen sensor green (SOSG) which reacts with SO generated from GV-Ce6.[9] The fluorescence intensity of SOSG at 528 nm increases with the prolonged irradiation, accompanied with a decrease in the fluorescence intensity of Ce6 at 662 nm (Figure 2d and Figure S9). The fluorescence intensities remain unaltered upon laser irradiation for systems with SOSG alone or a mixture of SOSG and GVs (Figure S10).

To assess the cellular uptake behavior and localization of GV-Ce6, human breast cancer cells (MDA-MB-435) were incubated with GVs (36.8 μg/mL), Ce6 (10 μM) and GV-Ce6 (10 μM Ce6, 36.8 μg/mL GVs). DAPI (4′,6-diamidino-2-phenylindole) staining was used to visualize nuclei. Figure 3a−o shows the fluorescence images of MDA-MB-435 cells incubated with GVs, Ce6, and GV-Ce6 (see low magnification images in Figure S11). For GVs exposure group, cells did not exhibit any red fluorescence signal. For cells incubated with free Ce6 or GV-Ce6 at the same Ce6 concentration, GV-Ce6 showed a stronger fluorescence signal inside cells than free Ce6 (Figure 3i−o and Figure S12), implying a possible better performance of using GV-Ce6 for PDT than that of using free Ce6, as PDT effect is strongly dependent on the uptake of PSs by tumor cells.

To quantify the cellular uptake efficiency of Ce6, fluorescence intensities of free Ce6 and GV-Ce6 in MDA-MB-435 cells were recorded on flow cytometry at different incubation time points (Figure 3p,q). The fluorescence intensity of Ce6 in both systems increased as a function of time (Figure 3r), while the GV-Ce6 group showed a significantly higher fluorescence intensity of Ce6 than free Ce6 group. The mean fluorescence intensity (4.46×10^5 au) of Ce6 in GV-Ce6 system was 47-fold stronger than that in free Ce6 system (9.2×10^3 au) after 0.5 h incubation. For GV-Ce6 group, the fluorescence intensity of Ce6 rapidly increased and saturated after 6 h. In contrast, the fluorescence intensity of Ce6 in free Ce6 group gradually increased in the course of 24 h. This indicates a more rapid and effective cellular uptake of GV-Ce6. This is because the internalization efficiency of GV-Ce6 through endocytosis is higher than that of free Ce6 through passive diffusion into cells. In addition, the encapsulation of Ce6 in GVs avoids the direct contact of Ce6 with cells during the circulation or internalization of

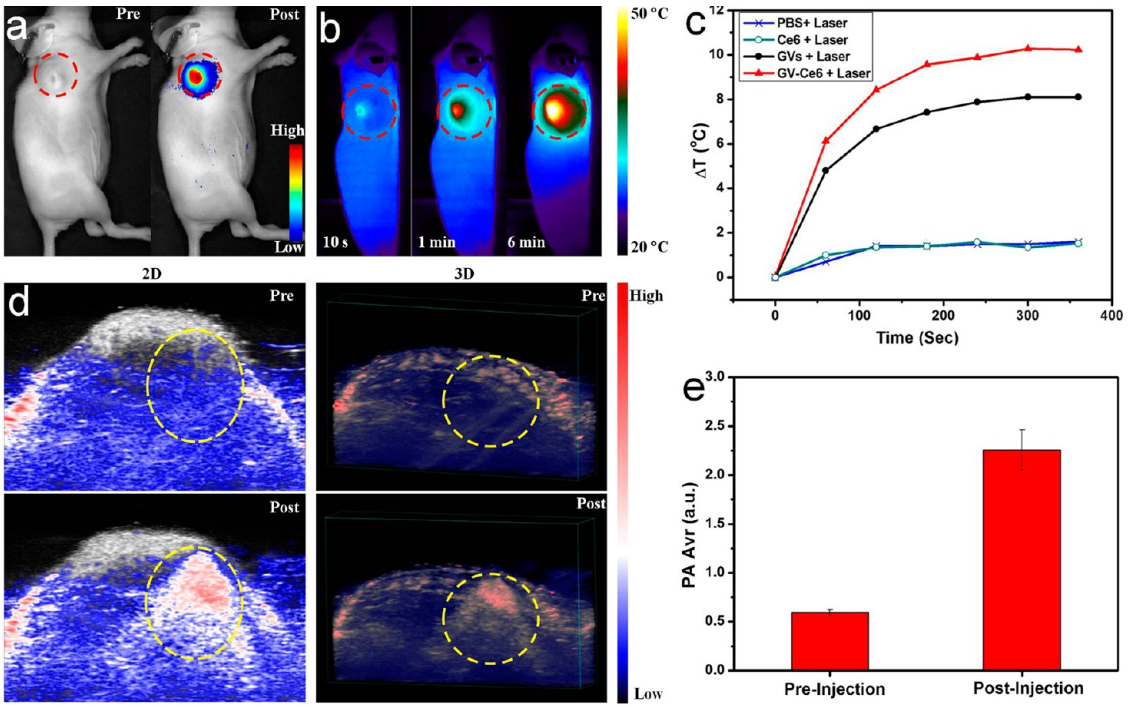

Figure 5. (a) *In vivo* NIR fluorescence image of MDA-MB-435 tumor-bearing mice at preinjection and postinjection of GV-Ce6. (b) Thermal images of tumor-bearing mice exposed to 671 nm laser (2.0 W/cm^2) for 6 min at postinjection of GV-Ce6. Red circles indicate the location of tumors. (c) Heating curves of tumors upon laser irradiation as a function of irradiation time. (d) *In vivo* photoacoustic (PA) images and (e) average PA intensity of tumor tissues at preinjection and postinjection of GV-Ce6. Yellow circles indicate the injected location.

Ce6 in biological systems, thus facilitating their biomedical application.

To verify the uptake mechanism of GV-Ce6, we incubated MDA-MB-435 cells with GV-Ce6 at low temperature (4 °C), which would inhibit the cellular endocytosis.[39−42] The fluorescent images showed that the uptake of GV-Ce6 was significantly depressed at 4 °C compared to that at 37 °C after 1 h, suggesting GV-Ce6 were internalized *via* energy-dependent endocytosis (Figure S13). To further study the subcellular localization of GV-Ce6, we used LysoTracker to stain lysosome and traced GV-Ce6 by a confocal laser scanning microscopy (CLSM). Figure S14 clearly showed the fluorescence signals from Lysotracker (green) match well with the fluorescence signals from GV-Ce6 (red), suggesting that majority of GV-Ce6 nanoparticles colocalized with the lysosomes, which is the fate of most nonviral vectors.[41,42] We suggest one possible endocytic pathway: GV-Ce6 was engulfed into cytoplasm and trafficked into the early endosomes, then into the late endosomes/lysosomes, and finally located in lysosomes.

Laser-triggered PTT/PDT effects of GVs, Ce6, and GV-Ce6 were analyzed by 3-(4,5-dimethyl-2-thiazolyl)-2,5-diphenyl-2*H*-tetrazolium bromide (MTT) assay. Cell viability was normalized by control group. The cell viability of irradiated groups gradually decreased with increasing the concentration of GVs, Ce6, and GV-Ce6 (Figure 4a and Figure S15). In contrast, the groups without laser irradiation exhibited negligible toxicity to MDA-MB-435 cells (Figure 4a). For treatment groups, the PDT/PTT efficacy of GV-Ce6 system is significantly improved, in comparison with GVs and free Ce6 systems at all the studied concentrations. The treatment efficacy of the GV-Ce6 system is about 45−70% higher than the sum effect of individual GVs and Ce6 system when 5% or 10% Ce6 was used (Figure S15). This result indicates that both synergistic PDT/PTT effect and enhanced cellular uptake are responsible for the improved therapeutic efficacy of GV-Ce6. In contrast, GNRs absorbed with Ce6 (GNR-Ce6) without irradiation exhibit obvious dark cytotoxicity within 5−20 μM, presumably due to the toxicity of cetyltrimethylammonium bromides (CTAB) on the surface of GNRs (Figure S16). For GNR-Ce6 with laser irradiation, the cytotoxicity is ascribed to both the toxicity of CTAB and the PDT/PTT effect, while the contribution of CTAB is more significant. After the subtraction of the toxicity of CTAB, GV-Ce6 showed a better performance in PDT/PTT than that of GNR-Ce6, owing to its good biocompatibility and high Ce6 loading efficiency.

The synergistic PDT/PTT effects of GV-Ce6 on MDA-MB-435 cells were further verified using Calcein AM and ethidium homodimer-1 co-staining. In the control group, cells all displayed green fluorescence, which suggests that laser irradiation alone cannot kill cells (Figure S17). In the GVs and Ce6 groups, some cells were killed and displayed red fluorescence (Figure 4b,c). In the GV-Ce6 group, without laser irradiation, cells

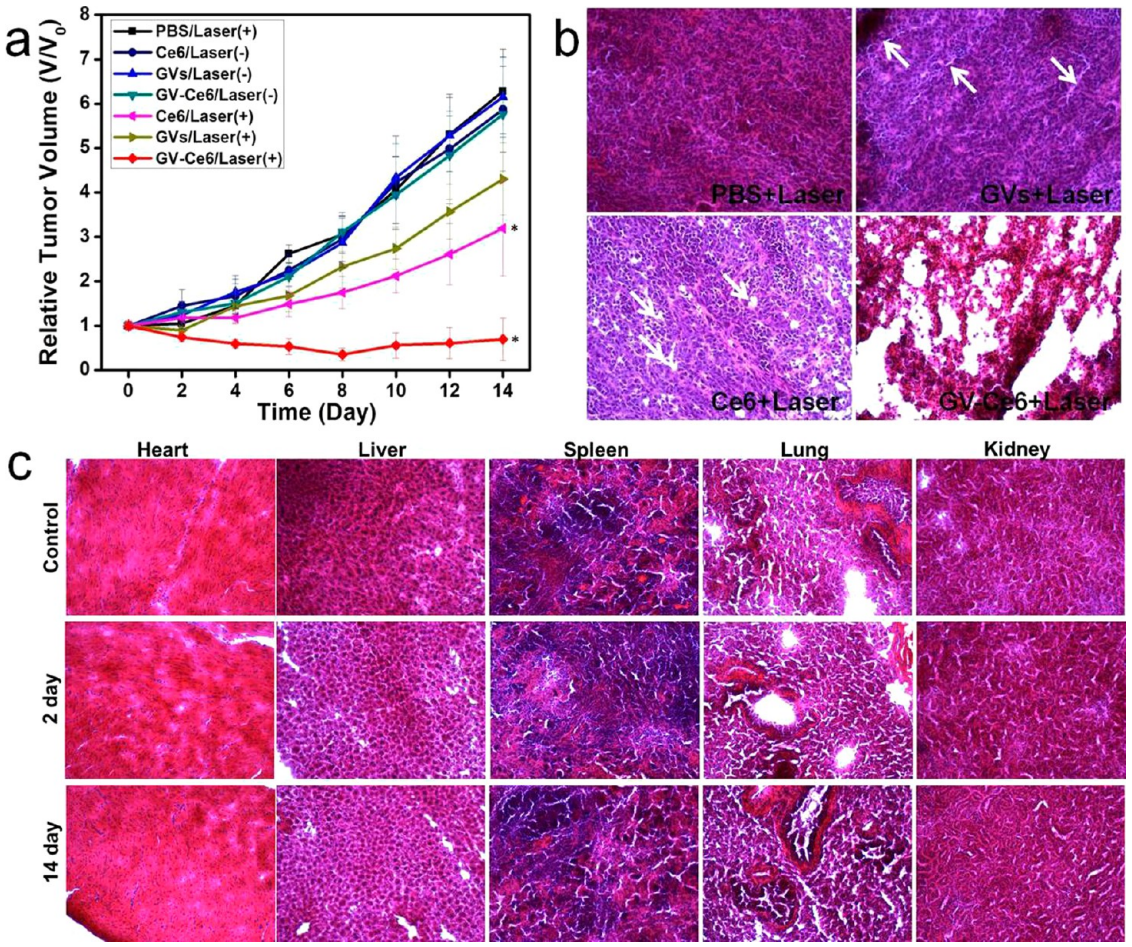

Figure 6. (a) Tumor growth curves of different groups of tumor-bearing mice after treatment. Tumor volumes were normalized to their initial sizes. Error bars represent the standard deviations of 4−6 mice per group. Asterisk indicates $P < 0.05$. (b) H&E stained tumor sections collected from different groups of mice 14 days post treatment. Arrows indicate the sporadic necrotic areas. (c) H&E stained images of major organs collected from control and GV-Ce6 administrated and irradiated mice at 2 and 14 days post treatment.

displayed green fluorescence, suggesting that GV-Ce6 is nontoxic to tumor cells in the dark (Figure S18a). Upon laser irradiation, all cells were killed, as indicated by the intense homogeneous red fluorescence (Figure 4d). The population of dead cells gradually increased with increased concentration of GV-Ce6 (Figure S18b−d). The PDT/PTT treatment using GV-Ce6 is highly selective and localized. Cells without irradiation (outside the region of laser spot) displayed green fluorescence, while cells were locally killed within irradiation region (Figure S19). The above results are in a good agreement with MTT assay.

We investigated the feasibility of using GV-Ce6 for *in vivo* trimodality fluorescence/thermal/PA imaging-guided synergistic PTT/PDT. Athymic nude mice with subcutaneous MDA-MB-435 breast cancer xenografts were selected as the animal model. When the size of tumors reached ~60 mm^3, the mice were intratumorally injected with 50 μL GV-Ce6 (100 μM Ce6). NIR fluorescence and PA imaging were employed to monitor the efficacy of treatment *in vivo*. After injection, intense fluorescence signal was observed in the tumor area (Figure 5a). Meanwhile, thermal images were recorded using an infrared thermal camera (Figure 5b). Upon laser irradiation, the local temperature of tumor rapidly increased to >42 °C, which is high enough to ablate the malignant cells. The surrounding healthy tissue showed negligible increase about 1−2 °C, while no significant temperature change was observed in other parts of the mice. No significant temperature rising was observed in other body parts of the mice. To confirm that the PTT effect was originated from the GV component in GV-Ce6, we also tested tumor injected with GVs or Ce6 (at the same dose as GV-Ce6) upon laser irradiation (Figure 5c). For GV-Ce6, the tumor temperature increased about 10 °C within 6 min, which is slightly higher than that of GVs, due to the absorbance of loaded Ce6 in GV-Ce6 at 671 nm (Figure S20). For Ce6 and PBS, the tumor tissues did not show any significant temperature changes (Figure S21). Intense PA signal was observed in the tumor region injected with GC-Ce6 (Figure 5d). The average PA intensity (2.25 ± 0.21 au) of GV-Ce6 was 3.8-fold stronger than that before particle injection (0.59 ± 0.03 au)

(Figure 5e). The fluorescence, thermal and PA signal were ascribed to the presence of GV-Ce6.

In vivo therapeutic efficacy of Ce6, GV and GV-Ce6 was assessed by monitoring the growth rate of tumors. The size of tumors was normalized to their initial size. Ce6, GV and GV-Ce6 administration/irradiation groups showed remarkable delay in tumor growth or tumor regression compared with the control group after two weeks (GVs *vs* Ctl, $P < 0.001$; Ce6 *vs* Ctl, $P < 0.0001$; GV-Ce6 *vs* Ctl, $P < 0.0001$) (Figure 6a). In contrast, the groups without laser irradiation showed no apparent change of tumor size compared with the control group, indicating the therapeutic effect was highly light-dependent. It is noteworthy that GV-Ce6 treated group exhibited higher therapeutic efficacy as compared with Ce6 and GV treated group on day 14 (GV-Ce6 *vs* GV, $P < 0.0001$; GV-Ce6 *vs* Ce6, $P < 0.0001$). These results clear demonstrated the synergistic effect of PDT/PTT over any single modality treatment solely. H&E staining of tumor sections was performed on day 14 in Figure 6b. In PBS, GVs, Ce6 treated group, the histological section showed infiltrating tumor cells with highly pleomorphic nuclei and many mitoses, indicating limited benefit from laser treatment. In contrast, intensive necrosis area stained by eosin dominated tumor section in GV-Ce6 treated group. Pyknosis can also be observed in GV-Ce6 treated tumor cells, resulting from irreversible condensation of chromation in the nuclei of tumor cells undergoing necrosis or apoptosis. Since part of the intratumoral injected nanoparticles would leak into circulation and prominently accumulate in reticuloendothelial system of spleen and liver,[43,44] we also collected major organs including heart, liver, spleen, lung and kidney from the mice at 2 days and 14 days after treatment (Figure 6c). Neither obvious damage nor inflammation was observed compared to the control group, probably resulting from the low cytotoxicity and immunogenicity of gold nanoparticles.[45] These results indicate that GV-Ce6 has excellent theranostic capability without noticeable toxicity, and is suitable for imaging-guided synergistic PTT/PDT of tumor *in vivo*.

CONCLUSION

In summary, we have developed a novel theranostic platform based on photosensitizer-loaded plasmonic vesicular assemblies for cancer imaging and treatment. The strong NIR absorption induced by plasmon coupling between adjacent GNPs and the capability of encapsulating active compounds such as Ce6 in GVs enables the trimodality NIR fluorescence/thermal/PA imaging-guided synergistic photothermal/photodynamic therapy with improved efficacy. The GV-Ce6 we developed shows the following characteristics: (i) high Ce6 loading efficiency in the hollow interior of GVs; (ii) enhanced delivery of Ce6 into cells; (iii) simultaneous trimodality NIR fluorescence/thermal/PA imaging; and (iv) synergistic PTT/PDT treatment with improved efficacy using single wavelength continuous wave laser irradiation. In addition, the multifunctional vesicular nanocarrier has high solubility and stability in aqueous solution, and good biocompatibility, thus facilitating its biomedical applications, particularly for cancer theranostics. To further improve the performance of the GV platform in bioimaging and drug delivery, more efforts shall be undertaken to: (i) accurately control the size of GVs in the range of 50−150 nm; (ii) tune the LSPR peak of GVs in the longer NIR range; (iii) use biodegradable polymers for assembly; (iv) modify the surface of GVs with specific biomarkers to achieve targeting purposes; and (v) systemically assess the toxicity, biocompability, pharmacokinetics and biodistribution of the GVs *in vivo*.

EXPERIMENTAL SECTION

Preparation of GV-Ce6. Plasmonic GVs were prepared by assembling GNPs tethered with amphiphilic block copolymers (BCPs) using film rehydration method. GNPs were prepared by citrate reduction of $HAuCl_4$ in aqueous phase. Briefly, GNPs were modified with thiol-terminated BCPs of polyethylene oxide-*b*-polystyrene (PEO_{45}-*b*-PS_{245}) (M_n = 25.7 kg/mol, PDI = 1.12). The self-assembly of the BCP-tethered GNPs was triggered by rehydration of a thin film of the GNPs dried on a glass substrate in water with sonication. To encapsulate Ce6 in the vesicles, an aqueous solution Ce6 with predetermined concentration of Ce6 was used as solvent for the rehydration process. After that, the solution was centrifuged at 9000 rpm for 5 min, decanted and suspended in ultra pure water or PBS for further characterization and application.

Characterization of GV-Ce6. The morphologies of assemblies were imaged using a Hitachi SU-70 Schottky field emission gun Scanning Electron Microscope (FEG-SEM) and a Tecnai TF30 TEM (FEI, Hillsboro, OR) equipped with a Gatan Ultrascan 1000 CCD camera (Gatan, Pleasaton, CA). Samples for SEM were prepared by casting a 5−10 μL of NP aqueous solution on silicon wafers, and dried at room temperature. TEM samples were prepared by casting a 5−10 μL of GVs aqueous solution on 300 mesh copper grids covered with carbon film, and dried at room temperature. Hydrodynamic diameter of GVs in ultra pure water was measured by a SZ-100 nanoparticle analyzer (HORIBA Scientific, Tokyo, Japan). UV−vis spectra were measured by a Genesys 10S UV−vis spectrophotometer (Thermo Scientific, Waltham, MA). Fluorescence intensity was monitored with an F-7000 fluorescence spectrophotometer (Hitachi, Tokyo, Japan). Thermal images were captured by a SC300 infrared camera (FLIR, Arlington, VA) and processed with Examin IR image software (FLIR). The excitation source was a 671 nm diode-pumped solid-state laser system (LASERGLOW Technologies, Toronto, Canada).

Ce6 Loading Efficiency Measurements. In the calibration curve, the absorption intensity is linearly proportional to the concentration of Ce6, following a regression equation: $Y = 0.146 + 0.028X$ ($R^2 = 0.9977$) (Figure S4). UV−vis measurements of GV-Ce6 at different concentrations were carried out. To estimate the amount of Ce6 loaded by GVs, the GV-Ce6 was collected by centrifugation, and the unconjugated Ce6 in the supernatant

was quantified by using Ce6 UV calibration curve at 663 nm (in PBS solution). Every experiment was repeated three times.

Single Oxygen Detection. Singlet oxygen sensor green (SOSG) was employed to evaluate the singlet oxygen generation (SOG) of GV-Ce6. A certain of GV-Ce6 was mixed with SOSG (1 μM) in water containing 2% methanol. The mixture solutions were irradiated with an NIR laser (671 nm, 2 W/cm^2). SOSG fluorescence was excited with a light resource of 494 nm wavelength. The SOG of samples was quantified by comparing the SOSG fluorescence enhancement with the background or control samples.

Light to Heat Conversion. Samples in Eppendorf tubes were irradiated upon an 808 nm laser at power density of 2W/cm^2. The laser spot was adjusted to cover the whole surface of samples. Real-time thermal imaging of samples was recorded using a FLIR thermal camera and quantified by FLIR Examiner software.

Subcellular Localization and Uptake Efficiency. MDA-MB-435 cells were plated at least 24 h before incubation with GV-Ce6 in LabTek II coverglass (Nalge Nunc Internationl, Rochester, NY) at a density of 5×10^4 cells/mL and grown to 60−80% confluence. The cells were incubated with GVs (36.8 μg/mL), Ce6 (10 μM) and GV-Ce6 (10 μM) in the dark for 2 h. After incubation, the cells were thoroughly washed three times with PBS. Images were acquired by a laser scanning confocal microscope (FLUOVIEW FV10i, Olympus). The fluorescence micrographs shown are representative of at least three independent experiments. For cellular uptake experiment, the cells (5×10^4 cells per well) were seeded in 6-well plates and incubated overnight, and then incubated with 10 μM GV-Ce6 or Ce6. After different incubation times (0.5, 1, 2, 6, and 24 h), cells were rinsed with PBS three times, tripsinized, and resuspended with medium. Afterward, the cells were collected by Accuir C6 flow cytometer using CFlow Plus software (BD, Ann Arbor, MI). All data was analyzed using 10 000 cells by FlowJo version 7.6.5 (FlowJo, Ashland, OR).

Laser-Induced Synergistic PTT/PDT Effect. MDA-MB-435 cells (1×10^4 cells per well) were seeded in 96-well plates and incubated overnight at 37 °C in a humidified 5% CO_2 atmosphere. After being rinsed with PBS (pH 7.4), the cells were incubated with GVs (0−73.6 μg/mL), Ce6 (0−20 μM) and GV-Ce6 (0−20 μM) for 12 h at 37 °C under the same conditions. Afterward, the cells of experimental group were rinsed again with PBS and immersed in 200 μL of fresh culture medium, and subsequently illuminated using a 671 nm laser with energy density of ~2 W/cm^2 for 3 min. The laser spot was adjusted to fully cover the area of each well. After illumination, cells were incubated for 24 h in a 5% CO_2, 95% air humidified incubator at 37 °C. Dark control group was keep under identical conditions as the experimental group except for illumination. The standard MTT assay was carried out to evaluate the cell viability.

The synergistic PDT/PTT effects of GV-Ce6 on MDA-MB-435 cells were further verified using Calcein AM and ethidium homodimer-1 co-staining. MDA-MB-435 cells (5×10^4 cells per well) were seeded in 6-well plates and incubated overnight at 37 °C in a humidified 5% CO_2 atmosphere. After being rinsed with PBS (pH 7.4), the cells were incubated with GVs (36.8 μg/mL), Ce6 (10 μM) and GV-Ce6 (10 μM Ce6, 36.8 μg/mL GVs) for 12 h at 37 °C under the same conditions and then irradiated with 671 nm laser at a power density of 2 W/cm^2 for 3 min.

***In Vivo* Fluorescence and Photoacoustic Imaging of GV-Ce6.** All animal operations were in accord with institutional animal use and care regulations. Tumor-bearing mice were prepared by subcutaneously injecting a suspension of 5×10^6 MDA-MB-435 cells in PBS (100 μL) into bilateral shoulders of female nude mice (six weeks old, 20−25 g). When the tumor size reached ~60 mm^3, 50 μL of GV-Ce6 (corresponding to 100 μM Ce6) was intratumorally injected into the tumor-bearing mice. The fluorescent scans were recorded on a Maestro all-optical imaging system (Caliper Life Sciences, Hopkinton, MA). Photoacoustic (PA) imaging was performed by a Vevo 2100 LAZR system (VisualSonics, Inc., New York, NY) equipped with a 40 MHz, 256-element linear array transducer on tumors.

***In Vivo* Thermal Imaging.** When the tumor size reached ~60 mm^3, 50 μL of GV-Ce6 (corresponding to 100 μM Ce6), 368 μg/mL GVs, or 100 μM Ce6 was intratumorally injected into the tumor-bearing mice. Thermal imaging was recorded by a SC300 infrared camera (FLIR) when the tumors were exposed to 671 nm laser (LASERGLOW Technologies) of power density at 2 W/cm^2.

***In Vivo* Phototoxicity Study.** When the tumor size reached ~60 mm^3, 50 μL of GV-Ce6 (corresponding to 100 μM Ce6), 368 μg/mL GVs, or 100 μM Ce6 was intratumorally injected into the tumor-bearing mice. MDA-MB-435 tumor-bearing mice were divided into 7 groups of five animals per group to quantify the growth rate of tumors after the following treatments: (a) PBS administrated and irradiated; (b) Ce6 administrated only; (c) GVs administrated only; (d) GV-Ce6 administrated only; (e) Ce6 administrated and irradiated; (f) GV administrated and irradiated; and (g) GV-Ce6 administrated and irradiated. For irradiated groups, the tumors were exposed to 671 nm laser of power density at 2 W/cm^2. The spot of laser beam was adjusted to cover the entire region of tumor. The size of tumors was measured by caliper every other day after the treatment. The volume of tumor (V) was calculated by the following equation: $V = A \cdot B^2/2$, where A and B are the longer and shorter diameter (mm) of the tumor, respectively. The relative volume of tumors was evaluated by normalizing the measured values to their initial sizes.

Conflict of Interest: The authors declare no competing financial interest.

Acknowledgment. This work was supported by the startup funds from the University of Maryland, the Intramural Research Program (IRP) of the National Institute of Biomedical Imaging and Bioengineering (NIBIB), National Institutes of Health (NIH), the National Key Basic Research Program (973 Project) (2010CB-933901 and 2013CB733802), the National Science Foundation of China (81272987, 31170961, 51102258), Zhejiang Province Foundation (LY12H11011), and the Chinese Academy of Sciences professorship for Senior International Scientists (2011T2J06).

Supporting Information Available: Details of physical, chemical and biological characterization of the gold nanovesicles. This material is available free of charge *via* the Internet at http://pubs.acs.org.

REFERENCES AND NOTES

1. Lovell, J. F.; Liu, T.; Chen, J.; Zheng, G. Activatable Photosensitizers for Imaging and Therapy. *Chem. Rev.* **2010**, *110*, 2839–2857.
2. Celli, J. P.; Spring, B. Q.; Rizvi, I.; Evans, C. L.; Samkoe, K. S.; Verma, S.; Pogue, B. W.; Hasan, T. Imaging and Photodynamic Therapy: Mechanisms, Monitoring and Optimization. *Chem. Rev.* **2010**, *110*, 2795–2838.
3. Rai, P.; Mallidi, S.; Zheng, X.; Rahmanzadeh, R.; Mir, Y.; Elrington, S.; Khurshid, A.; Hasan, T. Development and Applications of Photo-Triggered Theranostic Agents. *Adv. Drug Delivery Rev.* **2010**, *62*, 1094–1124.
4. Xie, J.; Lee, S.; Chen, X. Nanoparticle-Based Theranostic Agents. *Adv. Drug Delivery Rev.* **2010**, *62*, 1064–1079.
5. Kelkar, S. S.; Reineke, T. M. Theranostics: Combining Imaging and Therapy. *Bioconjugate Chem.* **2011**, *22*, 1879–1903.
6. Choi, K. Y.; Liu, G.; Lee, S.; Chen, X. Theranostic Nanoplatforms for Simultaneous Cancer Imaging and Therapy: Current Approaches and Future Perspectives. *Nanoscale* **2012**, *4*, 330–342.
7. Wang, J.; You, M.; Zhu, G.; Shukoor, M. I.; Chen, Z.; Zhao, Z.; Altman, M. B.; Yuan, Q.; Zhu, Z.; Chen, Y.; *et al.* Photosensitizer-Gold Nanorod Composite for Targeted Multimodal Therapy. *Small* **2013**, 10.1002/smll.201202155.
8. Kim, J.; Piao, Y.; Hyeon, T. Multifunctional Nanostructured Materials for Multimodal Imaging, and Simultaneous Imaging and Therapy. *Chem. Soc. Rev.* **2008**, *38*, 372–390.
9. Huang, P.; Lin, J.; Wang, X.; Wang, Z.; Zhang, C.; He, M.; Wang, K.; Chen, F.; Li, Z.; Shen, G. Light-Triggered Theranostics Based on Photosensitizer-Conjugated Carbon Dots for Simultaneous Enhanced-Fluorescence Imaging

and Photodynamic Therapy. *Adv. Mater.* **2012**, *24*, 5104–5110.
10. Dougherty, T. J.; Henderson, B. W.; Gomer, C. J.; Jori, G.; Kessel, D.; Korbelik, M.; Moan, J.; Peng, Q. Photodynamic Therapy. *J. Natl. Cancer Inst.* **1998**, *90*, 889–905.
11. Henderson, B. W.; Dougherty, T. J. How Does Photodynamic Therapy Work?. *Photochem. Photobiol.* **2008**, *55*, 145–157.
12. Tian, B.; Wang, C.; Zhang, S.; Feng, L.; Liu, Z. Photothermally Enhanced Photodynamic Therapy Delivered by Nano-Graphene Oxide. *ACS Nano* **2011**, *5*, 7000–7009.
13. Sun, Y.; Chen, Z.; Yang, X.; Huang, P.; Zhou, X.; Du, X. Magnetic Chitosan Nanoparticles as a Drug Delivery System for Targeting Photodynamic Therapy. *Nanotechnology* **2009**, *20*, 135102.
14. Wang, S.; Gao, R.; Zhou, F.; Selke, M. Nanomaterials and Singlet Oxygen Photosensitizers: Potential Applications in Photodynamic Therapy. *J. Mater. Chem.* **2004**, *14*, 487–493.
15. Bechet, D.; Couleaud, P.; Frochot, C.; Viriot, M. L.; Guillemin, F.; Barberi-Heyob, M. Nanoparticles as Vehicles for Delivery of Photodynamic Therapy Agents. *Trends Biotechnol.* **2008**, *26*, 612–621.
16. Huang, P.; Li, Z.; Lin, J.; Yang, D.; Gao, G.; Xu, C.; Bao, L.; Zhang, C.; Wang, K.; Song, H. Photosensitizer-Conjugated Magnetic Nanoparticles for *in Vivo* Simultaneous Magneto-fluorescent Imaging and Targeting Therapy. *Biomaterials* **2011**, *32*, 3447–3458.
17. Bonnett, R. Photosensitizers of the Porphyrin and Phthalocyanine Series for Photodynamic Therapy. *Chem. Soc. Rev.* **1995**, *24*, 19–33.
18. Huang, P.; Xu, C.; Lin, J.; Wang, C.; Wang, X.; Zhang, C.; Zhou, X.; Guo, S.; Cui, D. Folic Acid-Conjugated Graphene Oxide Loaded with Photosensitizers for Targeting Photodynamic Therapy. *Theranostics* **2011**, *1*, 240–250.
19. Huang, P.; Lin, J.; Yang, D.; Zhang, C.; Li, Z.; Cui, D. Photosensitizer-Loaded Dendrimer-Modified Multi-Walled Carbon Nanotubes for Photodynamic Therapy. *J. Controlled Release* **2011**, *152*, e33–e34.
20. Chen, Z. L.; Sun, Y.; Huang, P.; Yang, X. X.; Zhou, X. P. Studies on Preparation of Photosensitizer Loaded Magnetic Silica Nanoparticles and Their Anti-Tumor Effects for Targeting Photodynamic Therapy. *Nanoscale Res. Lett.* **2009**, *4*, 400–408.
21. Liu, F.; Zhou, X.; Chen, Z.; Huang, P.; Wang, X.; Zhou, Y. Preparation of Purpurin-18 Loaded Magnetic Nanocarriers in Cottonseed Oil for Photodynamic Therapy. *Mater. Lett.* **2008**, *62*, 2844–2847.
22. Hongying, Y.; Fuyuan, W.; Zhiyi, Z. Photobleaching of Chlorins in Homogeneous and Heterogeneous Media. *Dyes Pigm.* **1999**, *43*, 109–117.
23. Coutier, S.; Mitra, S.; Bezdetnaya, L. N.; Parache, R. M.; Georgakoudi, I.; Foster, T. H.; Guillemin, F. Effects of Fluence Rate on Cell Survival and Photobleaching in Meta-Tetra-(Hydroxyphenyl) Chlorin-Photosensitized Colo 26 Multicell Tumor Spheroids. *Photochem. Photobiol.* **2001**, *73*, 297–303.
24. Sitnik, T.; Hampton, J.; Henderson, B. Reduction of Tumour Oxygenation During and after Photodynamic Therapy *in Vivo*: Effects of Fluence Rate. *Br. J. Cancer* **1998**, *77*, 1386–1394.
25. Jang, B.; Choi, Y. Photosensitizer-Conjugated Gold Nanorods for Enzyme-Activatable Fluorescence Imaging and Photodynamic Therapy. *Theranostics* **2012**, *2*, 190–197.
26. Lovell, J. F.; Jin, C. S.; Huynh, E.; Jin, H.; Kim, C.; Rubinstein, J. L.; Chan, W. C. W.; Cao, W.; Wang, L. V.; Zheng, G. Porphysome Nanovesicles Generated by Porphyrin Bilayers for Use as Multimodal Biophotonic Contrast Agents. *Nat. Mater.* **2011**, *10*, 324–332.
27. Jang, B.; Park, J. Y.; Tung, C. H.; Kim, I. H.; Choi, Y. Gold Nanorod-Photosensitizer Complex for Near-Infrared Fluorescence Imaging and Photodynamic/Photothermal Therapy *in Vivo*. *ACS Nano* **2011**, *5*, 1086–1094.
28. Khlebtsov, B.; Panfilova, E.; Khanadeev, V.; Bibikova, O.; Terentyuk, G.; Ivanov, A.; Rumyantseva, V.; Shilov, I.; Ryabova, A.; Loshchenov, V. Nanocomposites Containing Silica-Coated Gold-Silver Nanocages and Yb-2, 4-Dimethoxyhematoporphyrin: Multifunctional Capability of Ir-Luminescence Detection, Photosensitization, and Photothermolysis. *ACS Nano* **2011**, *5*, 7077–7089.
29. Wang, J.; Zhu, G.; You, M.; Song, E.; Shukoor, M. I.; Zhang, K.; Altman, M. B.; Chen, Y.; Zhu, Z.; Huang, C. Z. Assembly of Aptamer Switch Probes and Photosensitizer on Gold Nanorods for Targeted Photothermal and Photodynamic Cancer Therapy. *ACS Nano* **2012**, *6*, 5070–5077.
30. Gao, L.; Fei, J.; Zhao, J.; Li, H.; Cui, Y.; Li, J. Hypocrellin Loaded Gold Nanocages with High Two-Photon Efficiency for the Photothermal/Photodynamic Cancer Therapy *in Vitro*. *ACS Nano* **2012**, *6*, 8030–8040.
31. Kuo, W. S.; Chang, C. N.; Chang, Y. T.; Yang, M. H.; Chien, Y. H.; Chen, S. J.; Yeh, C. S. Gold Nanorods in Photodynamic Therapy, as Hyperthermia Agents, and in near-Infrared Optical Imaging. *Angew. Chem., Int. Ed.* **2010**, *122*, 2771–2775.
32. Zhang, M.; Murakami, T.; Ajima, K.; Tsuchida, K.; Sandanayaka, A. S. D.; Ito, O.; Iijima, S.; Yudasaka, M. Fabrication of Znpc/Protein Nanohorns for Double Photodynamic and Hyperthermic Cancer Phototherapy. *Proc. Natl. Acad. Sci. U. A.* **2008**, *105*, 14773–14778.
33. Zhang, Z.; Wang, L.; Wang, J.; Jiang, X.; Li, X.; Hu, Z.; Ji, Y.; Wu, X.; Chen, C. Mesoporous Silica-Coated Gold Nanorods as a Light-Mediated Multifunctional Theranostic Platform for Cancer Treatment. *Adv. Mater.* **2012**, *24*, 1418–1423.
34. Nie, Z.; Petukhova, A.; Kumacheva, E. Properties and Emerging Applications of Self-Assembled Structures Made from Inorganic Nanoparticles. *Nat. Nanotechnol.* **2009**, *5*, 15–25.
35. Song, J.; Cheng, L.; Liu, A.; Yin, J.; Kuang, M.; Duan, H. Plasmonic Vesicles of Amphiphilic Gold Nanocrystals: Self-Assembly and External-Stimuli-Triggered Destruction. *J. Am. Chem. Soc.* **2011**, *133*, 10760–10763.
36. Song, J.; Zhou, J.; Duan, H. Self-Assembled Plasmonic Vesicles of Sers-Encoded Amphiphilic Gold Nanoparticles for Cancer Cell Targeting and Traceable Intracellular Drug Delivery. *J. Am. Chem. Soc.* **2012**, *134*, 13458–13469.
37. He, J.; Zhang, P.; Babu, T.; Liu, Y.; Gong, J.; Nie, Z. Near-Infrared Light-Responsive Vesicles of Au Nanoflowers. *Chem. Commun.* **2013**, *49*, 576–578.
38. He, J.; Liu, Y.; Babu, T.; Wei, Z.; Nie, Z. Self-Assembly of Inorganic Nanoparticle Vesicles and Tubules Driven by Tethered Linear Block Copolymers. *J. Am. Chem. Soc.* **2012**, *134*, 11342–11345.
39. Chithrani, B. D.; Chan, W. C. Elucidating the mechanism of cellular uptake and removal of protein-coated gold nanoparticles of different sizes and shapes. *Nano Lett.* **2007**, *7*, 1542–1550.
40. Chou, L. Y.; Ming, K.; Chan, W. C. Strategies for the intracellular delivery of nanoparticles. *Chem. Soc. Rev.* **2011**, *40*, 233–245.
41. Wang, F.; Wang, Y.-C.; Dou, S.; Xiong, M.-H.; Sun, T.-M.; Wang, J. Doxorubicin-tethered responsive gold nanoparticles facilitate intracellular drug delivery for overcoming multidrug resistance in cancer cells. *ACS Nano* **2011**, *5*, 3679–3692.
42. Carregal-Romero, S.; Ochs, M.; Rivera-Gil, P.; Ganas, C.; Pavlov, A. M.; Sukhorukov, G. B.; Parak, W. J. NIR-light triggered delivery of macromolecules into the cytosol. *J. Controlled Release* **2012**, *159*, 120–127.
43. Moon, H. K.; Lee, S. H.; Choi, H. C. *In vivo* near-infrared mediated tumor destruction by photothermal effect of carbon nanotubes. *ACS Nano* **2009**, *3*, 3707–3713.
44. Lammers, T.; Peschke, P.; Kühnlein, R.; Subr, V.; Ulbrich, K.; Huber, P.; Hennink, W.; Storm, G. Effect of intratumoral injection on the biodistribution and the therapeutic potential of HPMA copolymer-based drug delivery systems. *Neoplasia* **2006**, *8*, 788–795.
45. Salem, A. K.; Searson, P. C.; Leong, K. W. Multifunctional nanorods for gene delivery. *Nat. Mater.* **2003**, *2*, 668–671.